Multi-periodic nanostructures for photon control

Kluge, Christian; Adam, Jost; Barié, Nicole; Jakobs, Peter-Jürgen; Guttmann, Markus; Gerken, Martina

Published in:
Optics Express

DOI:
10.1364/OE.22.0A1363

Publication date:
2014

Document version
Final published version

Citation for pulished version (APA):
Kluge, C., Adam, J., Barié, N., Jakobs, P-J., Guttmann, M., & Gerken, M. (2014). Multi-periodic nanostructures for photon control. Optics Express, 22(S5), A1363-A1371. DOI: 10.1364/OE.22.0A1363

Multi-periodic nanostructures for photon control

Christian Kluge,[1] Jost Adam,[1,2] Nicole Barié,[3] Peter-Jürgen Jakobs,[3] Markus Guttmann,[3] Martina Gerken[1,*]

[1]*Institute of Electrical and Information Engineering, Christian-Albrechts-Universität zu Kiel (CAU), Kaiserstr. 2, D-24143 Kiel, Germany*

[2]*The Mads Clausen Institute, University of Southern Denmark (SDU), Alsion 2, DK-6400 Sønderborg, Denmark*

[3]*Institute of Microstructure Technology, Karlsruhe Institute of Technology (KIT), D-76344 Eggenstein-Leopoldshafen, Germany*

**mge@tf.uni-kiel.de*

Abstract: We propose multi-periodic nanostructures yielded by superposition of multiple binary gratings for wide control over photon emission in thin-film devices. We present wavelength- and angle-resolved photoluminescence measurements of multi-periodically nanostructured organic light-emitting layers. The spectral resonances are determined by the periodicities of the individual gratings. By varying component duty cycles we tune the relative intensity of the main resonance from 12% to 82%. Thus, we achieve simultaneous control over the spectral resonance positions and relative intensities.

OCIS codes: (050.5298) Photonic crystals; (260.5740) Resonance; (160.4236) Nanomaterials; (230.3670) Light-emitting diodes.

References and links

1. M. H. Crawford, "LEDs for Solid-State Lighting: Performance Challenges and Recent Advances," IEEE J. Sel. Top. Quantum Electron. **15**(4), 1028–1040 (2009).
2. V. Bulović, V. B. Khalfin, G. Gu, P. E. Burrows, D. Z. Garbuzov, and S. R. Forrest, "Weak microcavity effects in organic light-emitting devices," Phys. Rev. B **58**(7), 3730–3740 (1998).
3. S. Zhang, G. A. Turnbull, and I. D. W. Samuel, "Enhancing the emission directionality of organic light-emitting diodes by using photonic microstructures," Appl. Phys. Lett. **103**(21), 213302 (2013).
4. W. H. Koo, S. M. Jeong, F. Araoka, K. Ishikawa, S. Nishimura, T. Toyooka, and H. Takezoe, "Light extraction from organic light-emitting diodes enhanced by spontaneously formed buckles," Nat. Photonics **4**(4), 222–226 (2010).
5. A. David, H. Benisty, and C. Weisbuch, "Photonic crystal light-emitting sources," Rep. Prog. Phys. **75**(12), 126501 (2012).
6. L. Mahler, A. Tredicucci, F. Beltram, C. Walther, J. Faist, H. E. Beere, D. A. Ritchie, and D. S. Wiersma, "Quasi-periodic distributed feedback laser," Nat. Photonics **4**(3), 165–169 (2010).
7. J. Herrnsdorf, B. Guilhabert, Y. Chen, A. Kanibolotsky, A. Mackintosh, R. Pethrick, P. Skabara, E. Gu, N. Laurand, and M. Dawson, "Flexible blue-emitting encapsulated organic semiconductor DFB laser," Opt. Express **18**(25), 25535–25545 (2010).
8. Z. Yu, A. Raman, and S. Fan, "Fundamental limit of nanophotonic light trapping in solar cells," Proc. Natl. Acad. Sci. U.S.A. **107**(41), 17491–17496 (2010).
9. J. M. Lupton, B. J. Matterson, I. D. W. Samuel, M. J. Jory, and W. L. Barnes, "Bragg scattering from periodically microstructured light emitting diodes," Appl. Phys. Lett. **77**(21), 3340 (2000).
10. L. Tutt and J. F. Revelli, "Distribution of radiation from organic light-emitting diode structures with wavelength-scale gratings as a function of azimuth and polar angles," Opt. Lett. **33**(5), 503–505 (2008).
11. U. Geyer, J. Hauss, B. Riedel, S. Gleiss, U. Lemmer, and M. Gerken, "Large-scale patterning of indium tin oxide electrodes for guided mode extraction from organic light-emitting diodes," J. Appl. Phys. **104**(9), 093111 (2008).
12. E. R. Martins, J. Li, Y. Liu, V. Depauw, Z. Chen, J. Zhou, and T. F. Krauss, "Deterministic quasi-random nanostructures for photon control," Nat. Commun. **4**(4), 2665 (2013).
13. E. R. Martins, J. Li, Y. Liu, J. Zhou, and T. F. Krauss, "Engineering gratings for light trapping in photovoltaics: The supercell concept," Phys. Rev. B **86**(4), 041404 (2012).
14. J.-W. Kim, J.-H. Jang, M.-C. Oh, J.-W. Shin, D.-H. Cho, J.-H. Moon, and J.-I. Lee, "FDTD analysis of the light extraction efficiency of OLEDs with a random scattering layer," Opt. Express **22**(1), 498–507 (2014).

#211146 - $15.00 USD Received 17 Jun 2014; revised 11 Aug 2014; accepted 13 Aug 2014; published 21 Aug 2014

15. L. Dal Negro, C. J. Oton, Z. Gaburro, L. Pavesi, P. Johnson, A. Lagendijk, R. Righini, M. Colocci, and D. S. Wiersma, "Light transport through the band-edge states of Fibonacci quasicrystals," Phys. Rev. Lett. **90**(5), 055501 (2003).
16. A. Othonos, X. Lee, and R. M. Measures, "Superimposed multiple Bragg gratings," Electron. Lett. **30**(23), 1972–1974 (1994).
17. W.-C. Tan, J. Sambles, and T. Preist, "Double-period zero-order metal gratings as effective selective absorbers," Phys. Rev. B **61**(19), 13177–13182 (2000).
18. D. C. Skigin and R. A. Depine, "Diffraction by dual-period gratings," Appl. Opt. **46**(9), 1385–1391 (2007).
19. I. Balin, N. Dahan, V. Kleiner, and E. Hasman, "Bandgap structure of thermally excited surface phonon polaritons," Appl. Phys. Lett. **96**(7), 071911 (2010).
20. C. Kluge, M. Rädler, A. Pradana, M. Bremer, P.-J. Jakobs, N. Barié, M. Guttmann, and M. Gerken, "Extraction of guided modes from organic emission layers by compound binary gratings," Opt. Lett. **37**(13), 2646–2648 (2012).
21. R. F. Kazarinov and C. Henry, "Second-order distributed feedback lasers," IEEE J. Quantum Electron. **21**(2), 144–150 (1985).
22. T. Tamir and S. T. Peng, "Analysis and design of grating couplers," Appl. Phys. (Berl.) **14**(3), 235–254 (1977).
23. Y. Hirai, S. Harada, H. Kikuta, Y. Tanaka, M. Okano, S. Isaka, and M. Kobayasi, "Imprint lithography for curved cross-sectional structure using replicated Ni mold," J. Vac. Sci. Technol. B. **20**(6), 2867 (2002).
24. B. A. Sexton and R. J. Marnock, "Characterization of High Resolution Resists and Metal Shims by Scanning Probe Microscopy," Microsc. Microanal. **6**(2), 129–136 (2000).
25. C. Vannahme, S. Klinkhammer, A. Kolew, P.-J. Jakobs, M. Guttmann, S. Dehm, U. Lemmer, and T. Mappes, "Integration of organic semiconductor lasers and single-mode passive waveguides into a PMMA substrate," Microelectron. Eng. **87**(5–8), 693–695 (2010).
26. M. Hansen, M. Ziegler, H. Kohlstedt, A. Pradana, M. Rädler, and M. Gerken, "UV capillary force lithography for multiscale structures," J. Vac. Sci. Technol. B. **30**(3), 031601 (2012).
27. M. G. Moharam, E. B. Grann, D. A. Pommet, and T. K. Gaylord, "Formulation for stable and efficient implementation of the rigorous coupled-wave analysis of binary gratings," J. Opt. Soc. Am. A **12**(5), 1068–1076 (1995).
28. D. L. Brundrett, E. N. Glytsis, T. K. Gaylord, and J. M. Bendickson, "Effects of modulation strength in guided-mode resonant subwavelength gratings at normal incidence," J. Opt. Soc. Am. A **17**(7), 1221–1230 (2000).

1. Introduction

Light-emitting diodes (LEDs) and organic light emitting diodes (OLEDs) are on their way to replace traditional light sources such as incandescent lamps and gas-discharge lamps [1]. LEDs and OLEDs allow for high efficiency and a compact form factor. Additionally, they offer unique opportunities in tailoring the emission profile. The light-emitting thin-film stack forms a microcavity [2], which may be used to enhance emission in particular angular directions. More control is obtained by integration of nanostructures close to the thin-film light-emitting layer, which enables emission characteristics far beyond standard Lambertian emission [3]. Generally, planar nanostructures are of high interest for controlling the emission and absorption of photons in thin-film devices such as light-emitting diodes (LEDs) [4,5], distributed-feedback (DFB) lasers [6,7], and solar cells [8]. A standard photonic crystal slab is a periodic nanostructure with a dominant space frequency responsible for a single resonance of the electromagnetic field. It allows for coupling of guided modes to radiation modes with a dominant wavelength-dependent emission (and absorption) direction depending on the grating period [9–11]. Recent reports [4,6,12,13] demonstrate that, if control in a wide range of wavelengths and angles is desired, nanostructures providing multiple resonances are beneficial. The application-specific benefit of multiple resonances depends critically on the ability to control their wavelength, emission angle, and intensity. A random nanostructure can be considered the limiting case providing an infinite number of infinitely weak resonances. While it is useful for enhancing the outcoupling efficiency in emissive devices [14], it does not provide emission profile control. In the regime between perfectly periodic and perfectly random nanostructures, quasi-crystalline [6,15], quasi-random [4,12], and superimposed periodic structures [16–20] have been shown to provide multiple resonances. Nevertheless, methods for controlling the resonance intensities are rare.

Here, we demonstrate that the superposition of multiple component gratings with different duty cycles allows for a rich Fourier spectrum and enables deterministic control over the relative resonances' strengths. Section 2 briefly introduces the multi-periodic nanostructure

#211146 - $15.00 USD Received 17 Jun 2014; revised 11 Aug 2014; accepted 13 Aug 2014; published 21 Aug 2014

and the proposed control over its Fourier spectrum. After description of the experimental methods in Section 3, we present wavelength- and angle-resolved photoluminescence measurements of multi-periodic nanostructures in a thin organic light-emitting layer in Section 4. We demonstrate that the resonances' relative intensities change with the component gratings' duty cycles, which agrees with our theoretical calculations. Finally, Section 5 concludes the paper.

2. The multi-periodic nanostructure

The multi-periodic nanostructure is constructed by a logical disjunction superposition of N binary single-periodic gratings as shown exemplarily for two component gratings in Fig. 1.

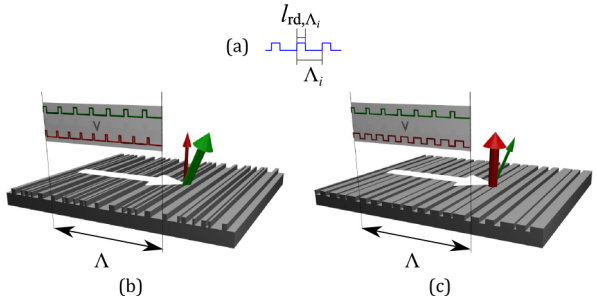

Fig. 1. Schematic and working principle of multi-periodic nanostructures. Multi-periodic nanostructures are constructed by superimposing multiple binary gratings using a logical disjunction operation. (a) The component gratings have periods Λ_i and ridge widths $l_{rd,\Lambda i}$ giving duty cycles of $l_{rd,\Lambda i}/\Lambda_i$. (b),(c) The resulting multi-periodic nanostructure is again a binary grating with period Λ that is the least common multiple of the component gratings' periods. The component gratings' periods determine the resonances' emission wavelengths and angles. The relative resonances' intensities are controlled by the duty cycles as shown schematically for the case of two different two-component gratings (b,c).

Due to the component gratings' periodicity, their Fourier spectra are discrete. For the component gratings' periods Λ_i, $i \in \{1,\ldots,N\}$, the multi-periodic nanostructure is also periodic, with the least common multiple (LCM) $\Lambda = \mathrm{LCM}\{\Lambda_1,\ldots, \Lambda_N\}$ being the period. Consequently, its Fourier spectrum is discrete and we use m to denote the Fourier order. The Fourier order $m = m_i\Lambda/\Lambda_i$ corresponds to the Fourier order m_i of the component grating with period Λ_i and is strong for the dominant component gratings' Fourier orders, if the component gratings' overlap is limited. As an example we consider a nanostructure with two component gratings with periods of 350 nm and 450 nm. We will denote this structure by 350|450. This multi-periodic nanostructure has a period of Λ = 3150 nm.

Figure 2(a) shows the power Fourier transform for ridge widths of $l_{rd,350nm}$ = 100 nm for the 350-nm component grating and $l_{rd,450nm}$ = 100 nm for the 450-nm component grating. Although the resulting period is much larger than the light wavelength in the visible regime, the multi-periodic nanostructure still comprises its components' dominating space frequencies. The 7th and 9th order correspond to the first Fourier orders of the 450-nm component and the 350-nm component grating, respectively. Their strengths are reduced compared to the single-period gratings due to the superposition.

#211146 - $15.00 USD Received 17 Jun 2014; revised 11 Aug 2014; accepted 13 Aug 2014; published 21 Aug 2014

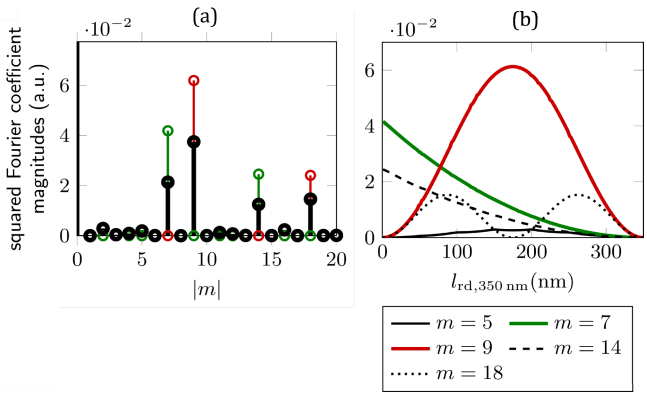

Fig. 2. Fourier spectrum of a two-periodic nanostructure. (a) Calculated power Fourier spectrum of a 350|450 ($l_{\mathrm{rd,350nm}}$ = 100 nm, $l_{\mathrm{rd,450nm}}$ = 100 nm) multi-periodic nanostructure (black) together with the involved single period component spectra (red and green). The multi-periodic nanostructure spectrum comprises the dominant Fourier orders of the component gratings. (b) Control of Fourier spectrum of the 350|450 multi-periodic nanostructure for varying $l_{\mathrm{rd,350nm}}$ and fixed $l_{\mathrm{rd,450nm}}$ = 100 nm. The ridge width $l_{\mathrm{rd,350nm}}$ of the 350-nm component grating provides wide control over the dominating Fourier orders 7 and 9.

2.1 Fourier spectrum control

It is well known that the duty cycle of a single-period grating controls the coupling efficiency to a specific emission angle [21]. Thus, we propose the choice of the duty cycles of the grating components prior to the superposition as a means to control the Fourier spectrum of the multi-periodic nanostructure. The *i*-th component's duty cycle is defined by the ratio of the ridge width $l_{\mathrm{rd},\Lambda i}$ and the component's period Λ_i (Fig. 1(a)). Figure 2(b) exemplarily shows the influence of the ridge width $l_{\mathrm{rd,350nm}}$ on the strongest Fourier coefficients of the 350|450 multi-period nanostructure, for a fixed ridge width $l_{\mathrm{rd,450nm}}$ = 100 nm. The 9th-order Fourier coefficient exhibits a bell-shaped curve with its maximum at $l_{\mathrm{rd,350nm}}$ = 175 nm, which corresponds to the component's duty cycle of 0.5. This curve behavior is well known for the first Fourier order of single-period binary gratings and is the reason why many binary grating waveguides radiate strongest close to a duty cycle of 0.5 [22]. Simultaneously, the 7th-order Fourier coefficient decreases with increasing $l_{\mathrm{rd,350nm}}$.

3. Experimental methods

In order to verify our theoretical findings, we experimentally investigated the resonant scattering of a guided mode in a nanostructured organic light-emitting layer.

3.1 Nanostructure fabrication

We fabricated 16 different multi-periodic nanostructures, each of 500 µm·500 µm size, on a single nickel shim. Initially, the structures were electron beam written (exposure dose 550 µC/cm^2; beam current 7 nA) in a 50-nm-thick poly(methyl methacrylate) (PMMA950k) layer on a silicon wafer. Subsequently, the structures were developed by a spray developer with a mixture of methyl isobutyl ketone and iso-propyl alcohol (MIBK:IPA 1:3). On top of the PMMA layer, a 7-nm-thick chromium layer and 15-nm-thick gold layer were evaporated, to act as adhesive layer and conducting base plate, respectively. In contrast to the commonly used >100 nm plating base layer thickness [23,24], we used a very thin plating base to avoid a planarization of the structures. This is especially important to fabricate the small feature sizes and depths down to 50 nm. Subsequently, approximately 0.5 mm nickel was deposited on the metallic layers by electroplating using a nickel sulphamate electrolyte similar to the process described by Vannahme et al. [25]. To ensure a slow nickel growth, to achieve a defect-free structure cavity filling, and to avoid problems with contacting the very thin metallization

#211146 - $15.00 USD Received 17 Jun 2014; revised 11 Aug 2014; accepted 13 Aug 2014; published 21 Aug 2014

layers, plating was started with very low current density (0.05 A/dm^2). During plating time, the current was increased up to 1.0 A/dm^2 (corresponding to a nickel growth speed of 12 µm/h). Finally, the silicon and the PMMA were removed, yielding a nickel shim with the nanostructures on its surface. A good structure quality was established, as shown in Fig. 3 by the scanning electron microscopy (SEM) image and atomic force microscopy (AFM) image.

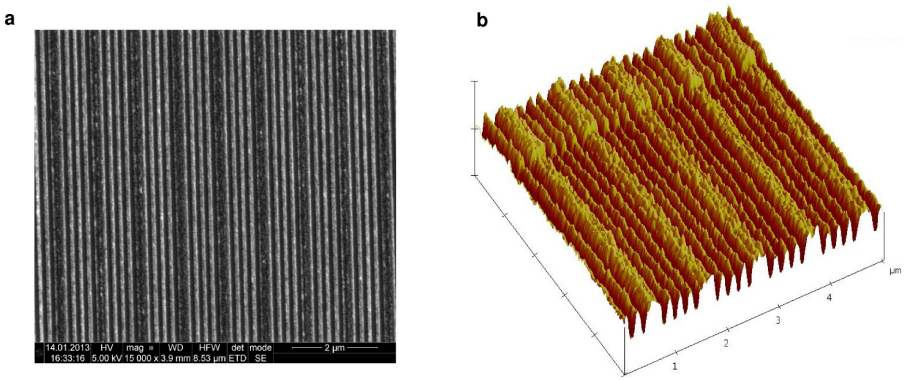

Fig. 3. Characterization of the nickel nanostructures by scanning electron microscopy (SEM) and atomic force microscopy (AFM). Exemplarily shown is a multi-periodic grating of type 196|400. (a), SEM image. (b), AFM height profile.

3.2 Sample fabrication

The nanostructures were transferred from the nickel shim to the samples using an established nanoimprint lithography (NIL) process [26]. For the replication stamp we used Sylgard 184 (Dow Corning Corporation) polydimethylsiloxane (PDMS), mixed in a basis-to-curing-agent ratio of 8:1 and cured at 80 °C for 135 min. Cleaned, quadratic float glass (25 mm·25 mm, 1 mm thick) provided the substrates for the samples. As NIL imprint resist, a 200-nm-thick layer of the UV-curable Amonil (AMO GmbH) was spin-coated onto the substrate, with prior application of Amoprime (AMO GmbH) to improve the adhesion between the glass substrate and the imprint layer. By application of the previously fabricated PDMS stamp onto the sample, without additional pressure, the nanostructure was transferred to the imprint resist. After curing the imprint layer under an UV-lamp for three minutes, the PDMS stamp was removed. As a result of the twofold transfer from the nickel shim to the PDMS stamp, and finally to the imprint resist, the imprint resist is structured equally to the nickel shim. Thereafter, a 65-nm-thick layer of the conjugated polymer Superyellow (Merck KGaA), a phenylene substituted poly(para-phenylenevinylene) derivative, was spin-coated onto the structured imprint resist. This step was done in a glovebox with inert nitrogen atmosphere to protect the Superyellow from oxygen and moisture. Finally, a 70-nm-thick silicon monoxide high-index and protection layer was deposited onto the Superyellow by thermal evaporation (0.12 nm s^{-1} evaporation rate). Thus, we obtained a 135-nm-thick, emissive waveguide layer on a substrate with 16 different multi-periodic nanostructures. The structure depth is approximately 30 nm, as determined by the structure depth on the nickel shim.

3.3 Emission measurements and normalization

For characterization of the sample emission, we focused a diode laser (15 mW, λ_0 = 405 nm) on the sample with a spot size of 256 µm horizontally, and 214 µm vertically ($1/e^2$-irradiance values), to separately excite the different nanostructures. We recorded the TE-polarized photoluminescence spectrally- and angularly-resolved in a plane perpendicular to the grating grooves. The sample was mounted on a rotational stage (Newport URS75BPP, ± 0.015° absolute accuracy), and was adjusted for each measurement such that the analyzed

#211146 - $15.00 USD Received 17 Jun 2014; revised 11 Aug 2014; accepted 13 Aug 2014; published 21 Aug 2014

nanostructure was not translated during rotation. A multi-mode fiber (205 µm diameter, 0.22 numerical aperture) collected the sample's photoluminescence at a distance of 50 mm, resulting in a full-width half-maximum (FWHM) angular resolution of ~0.3° to 0.6°. A spectrometer (Andor Shamrock SR-500i), together with a cooled back-illuminated charge-coupled device (CCD) detector (Andor DU920P-OE, at –60 °C), recorded the spectra with 0.75 s integration time. A TE polarization filter limited the measurement to the electric field normal to the plane of incidence.

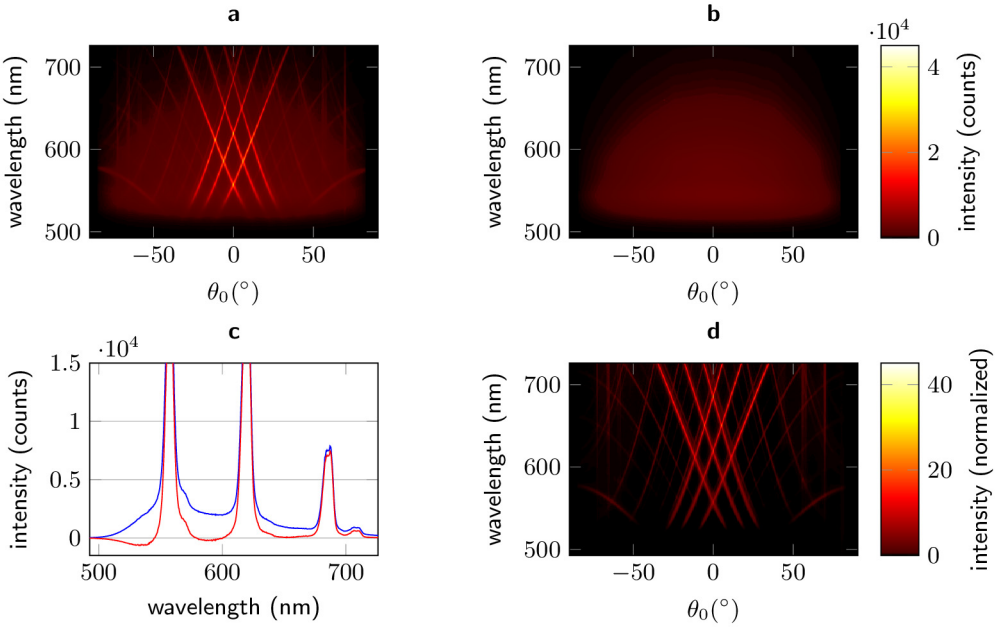

Fig. 4. Background removal and normalization of the emission spectrum. (a) Angularly- and spectrally-resolved, TE-polarized photoluminescence measurement of a nanostructured area on the sample. (b) TE-polarized photoluminescence measurement of an unstructured area on the sample. Multiplied with a matching factor, this emission is assumed to be the background of (a). (c) Background removal: measured signal (blue line) and background-free signal (red line) (TE-polarization, $\theta_0 = 0°$). The guided mode outcoupling peaks are approximately separated by subtracting the background. Note that the plotted intensity range has been limited. (d) Normalization. To obtain excitation-independent resonance peaks, the background-free emission spectrum is subsequently divided by the background spectrum at 0°.

The recorded photoluminescence from nanostructured areas on the sample comprises directly emitted light (background signal) and scattered light from the guided modes (resonance peaks) (see Fig. 4). Most resonance peaks are clearly visible in the raw measurements (Fig. 4(a)). We nevertheless chose to subtract the background, in order to improve the weak resonances' visibility in the following resonance peak analysis. The background signal is the part of the emission that does not emerge from guided mode scattering, but is emitted directly. We assumed that the background signal from the nanostructured waveguide is equal to the unstructured waveguide emission. Note that, by this assumption, we neglect the nanostructure's influence on the dipole emission. We measured the unstructured waveguide emission (see Fig. 4(b)) separately for each sample, at an unstructured area, with the same angular and spectral discretization and polarization as the grating areas. To match the background intensity in the nanostructured area with the intensity in the unstructured area, we integrated the intensity in a region of typically 5° angle and 7 nm wavelength and determined the ratio as a matching factor. The region was chosen individually for each grating, as it has to be uninfluenced by the peaks but exhibit sufficient background

#211146 - $15.00 USD Received 17 Jun 2014; revised 11 Aug 2014; accepted 13 Aug 2014; published 21 Aug 2014

intensity. For the emission depicted in Fig. 4(a), the matching region is centered at $\theta_0 = 0°$ and $\lambda_0 = 585$ nm. Subtraction of the intensity-matched background signal approximately leads to a separation of the scattered guided mode light and hence to isolated peaks in the spectrum as shown in Fig. 4(c). In order to obtain excitation-independent resonance intensities, the background-free emission was subsequently normalized to the background spectrum at 0° (see Fig. 4(d)). Note, however, that silicon monoxide intrinsic absorption influences the resonance intensities. To minimize fabrication-induced variations, all data in this paper have been measured with the same sample at adjacent nanostructured areas.

4. Resonance intensity control

4.1 Experimental results

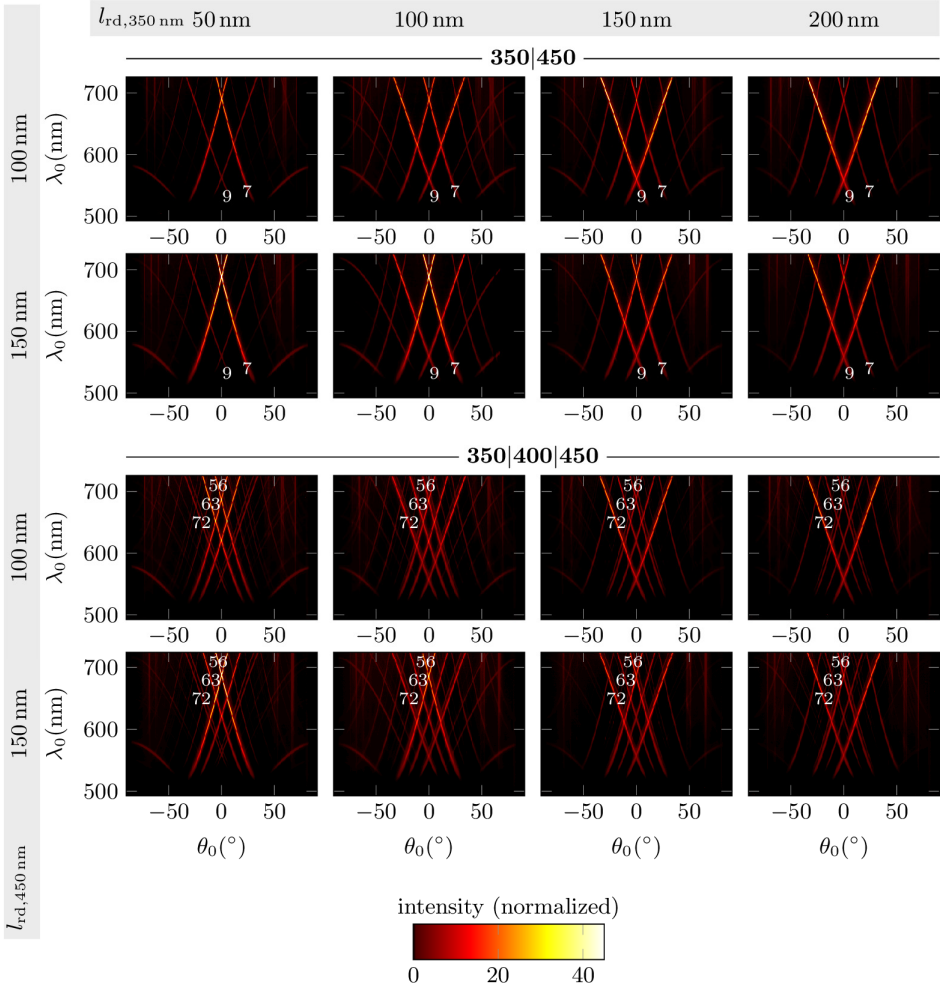

Fig. 5. Photoluminescence measurements of resonant scattering of the TE_0 guided mode at 16 different multi-periodic nanostructures. Shown is the normalized emission intensity as a function of wavelength and emission angle perpendicular to the grating grooves (continuous background subtracted and normalized). Symmetric pairs of peaks arise due to the presence of forward- and backward-traveling modes. The numbers next to the strongest peaks indicate the scattering order *m*. Note how the introduction of an additional component grating in the lower two rows leads to an additional pair of peaks. The ridge widths of the component gratings are varied along the columns and rows of the figure and provide control over the intensity of the resonances.

#211146 - $15.00 USD Received 17 Jun 2014; revised 11 Aug 2014; accepted 13 Aug 2014; published 21 Aug 2014

The two top rows of Fig. 5 show the normalized photoluminescence for multi-periodic nanostructures composed of two grating components (Λ_1 = 350 nm, Λ_2 = 450 nm; 350|450) and the two lower rows for a superposition of three grating components (Λ_1 = 350 nm, Λ_2 = 400 nm, Λ_3 = 450 nm; 350|400|450). The peaks arise from resonant scattering of the TE_0 mode, for which a transfer matrix simulation yields an effective refractive index n_{eff} between 1.69 at 510 nm wavelength and 1.53 at 710 nm wavelength. The peak positions in Fig. 5 are in agreement with the Bragg equation

$$\sin\theta_0 = n_{\text{eff}} - m\frac{\lambda_0}{\Lambda}, \tag{1}$$

where θ_0 denotes the scattering angle in air and λ_0 is the free-space wavelength. Note that n_{eff} depends on the average refractive index in the grating region, that is, the corresponding zero-order Fourier component, determined by the component gratings' duty cycles. For the present grating setups, n_{eff} differs less than 0.03 at a fixed wavelength as obtained by matching the measured angles θ_0 to Eq. (1). We recall that the first-order Fourier coefficients of the 350-nm and 450-nm component grating are at the orders 9 and 7, respectively, in the spectrum of the 350|450 multi-periodic nanostructure. The 350|400|450 multi-periodic nanostructure possesses a period of Λ = 25200 nm, such that the first-order Fourier coefficients of the 350-nm, 400-nm, and 450-nm component gratings are at the orders 72, 63, and 56, respectively. As observed in Fig. 5, the orders corresponding to the first Fourier coefficients of the component gratings lead to the strongest resonances as also seen in the theoretical results.

To demonstrate the deterministic control over the relative resonance intensities, we increased $l_{\text{rd,350nm}}$ in 50 nm steps from 50 nm to 200 nm (columns of Fig. 5). Up to $l_{\text{rd,350nm}}$ = 150 nm, the increased 350-nm component duty cycle leads to a steep increase of the corresponding resonance intensity. This is associated with the increasing 7th-order Fourier coefficient (see Fig. 2). For the further increase of $l_{\text{rd,350nm}}$ to 200 nm, the resonance intensity of the 9th and 72nd order are nearly constant, which can be explained by the nearly equal Fourier coefficients of these orders at $l_{\text{rd,350nm}}$ = 150 nm and $l_{\text{rd,350nm}}$ = 200 nm. Along the rows of Fig. 5, we compare two different values of $l_{\text{rd,450nm}}$. Clearly, an increase of $l_{\text{rd,450nm}}$ leads to increased resonance intensity associated with the 450-nm component, i.e., of the orders 7 and 56.

4.2 Comparison with simulation results

We implemented the rigorous coupled wave analysis (RCWA), as described by Moharam et al. [27], and added an additional waveguide layer. The quasi-guided modes were found by resonant excitation [28], such that RCWA yields the scattered plane wave intensities in the superstrate (air) and substrate (glass). We analyzed the following stack: [air(n = 1.00), 105 nm film (n = 1.93@λ_0 = 550 nm to n = 1.82@λ_0 = 700 nm), 30 nm grating, Amonil/glass (n = 1.52)], where film represents both the organic emitter and the silicon monoxide. We obtained the film refractive index by matching the measured scattering directions to the simulation results for each wavelength. The reference base for the relative peak intensities in Fig. 6 is the summed intensity of all scattering orders leaving the substrate, neglecting the scattering to the superstrate.

#211146 - $15.00 USD Received 17 Jun 2014; revised 11 Aug 2014; accepted 13 Aug 2014; published 21 Aug 2014

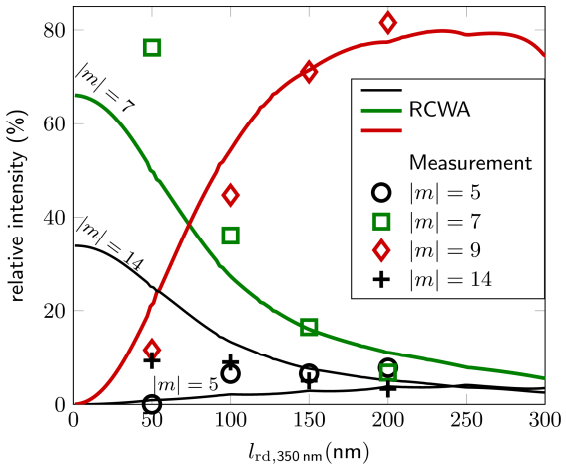

Fig. 6. Control of the peak intensities by a 350|450 multi-periodic nanostructure. Relative peak intensities with varying ridge width $l_{\mathrm{rd,350nm}}$ of the 350-nm component. The ridge width of the 450-nm component is 100 nm and the wavelength is λ_0 = 550 nm.

Figure 6 plots the experimentally observed relative resonance peak intensities for the 350|450 multi-periodic nanostructure, for varying $l_{\mathrm{rd,350nm}}$ and fixed $l_{\mathrm{rd,450nm}}$ = 100 nm, and demonstrates the agreement with rigorous coupled wave analysis (RCWA) simulation results. By appropriately choosing the 350-nm component grating duty cycle, the relative intensities of the two dominating resonances, i.e., orders 7 and 9, can be controlled in a wide range of values. Specifically, in the experimental results, the relative intensity of the 9th order was varied between 12% ($l_{\mathrm{rd,350nm}}$ = 50 nm) and 82% ($l_{\mathrm{rd,350nm}}$ = 200 nm).

5. Conclusion

We have demonstrated a method to construct a multi-periodic nanostructure that provides multiple strong resonances with simultaneous control over the resonance intensities. We considered the specific example of tailoring the light emission profile from a thin emissive film as it is found in LEDs or OLEDs. The concepts presented here are also applicable to light extraction from waveguides in general and to resonant light absorption.

Acknowledgments

The authors gratefully acknowledge support of the Bundesministerium für Bildung und Forschung (BMBF) within the project “NanoFutur” (03X5514). The authors thank M. Paulsen (CAU) for help with the measurements as well as J. Greve (CAU), B. Matthis (KIT), and M. Wissmann (KIT) for technical support. This work was carried out with the support of the Karlsruhe Nano and Micro Facility (KNMF, www.kit.edu/knmf), a Helmholtz Research Infrastructure at Karlsruhe Institute of Technology (KIT, www.kit.edu).